Title

Regulating the mechanical behavior of metamaterial microlattices by tactical structure modification

Authors

Vangelatos, Z
Komvopoulos, K
Grigoropoulos, CP

Publication Date

2020-11-01

DOI

10.1016/j.jmps.2020.104112

Peer reviewed

Journal of the Mechanics and Physics of Solids 144 (2020) 104112

Contents lists available at ScienceDirect

Journal of the Mechanics and Physics of Solids

journal homepage: www.elsevier.com/locate/jmps

Regulating the mechanical behavior of metamaterial microlattices by tactical structure modification

Z. Vangelatos, K. Komvopoulos*, C.P. Grigoropoulos*

Department of Mechanical Engineering, University of California, Berkeley, CA 94720, USA

ARTICLE INFO

Article history:
Received 26 March 2020
Revised 15 July 2020
Accepted 11 August 2020
Available online 13 August 2020

Keywords:
Architected microstructures
Buckling
Collapse
Deformation
Mechanical metamaterials
Microlattices
Microscopy
Multiphoton laser lithography
Nanoindentation

ABSTRACT

Microlattice structures possess properties imparted by the architected microstructure of their constituents (unit cells) and micro/nanofeatures rather than their bulk material properties. Post-processing techniques have revealed intriguing length scale effects, encompassing enhanced behavior or shape morphing of various structures. Although monolithic structures consisting of single unit cells have been successfully fabricated by advanced additive manufacturing techniques, such as multiphoton lithography, innovations towards the tactical architecture of localized failure and design-inherent controllable collapse have been fairly limited. Using as a point of reference the octet truss structure, we designed substitutional unit cells and slip-plane defect-like features inspired by crystalline materials. Through finite element analysis, we investigated how the directional effective stiffness of a material can be augmented and altered in predetermined orientations. Fabricating these structures by multiphoton laser lithography and testing them by in situ scanning electron microscopy-nanoindentation we discovered a remarkable enhancement of the structural integrity, stiffness, and strain energy density, emulating the corollaries of hardening bulk materials. In addition, we observed that these structures demonstrate localized plastic deformation and collapse, distinguishing their mechanical behavior from the conventional layer-by-layer collapse reported in previous studies. The nanofeatures detected in fractographies obtained by helium ion microscopy provided further insight into the collapse mechanisms of the structures. The present design methodology of strategically placed structural features yields architected microstructures with microlattice geometries that can be used to enhance and control the mechanical performance of metamaterial structures.

1. Introduction

Advances in additive manufacturing have led to the fabrication of architected materials with unprecedented properties. Characteristic examples are metamaterial structures demonstrating controllable wave propagation (Berezovski et al., 2020) or nonlinear recoverable large deformations (Yildizdag et al., 2019). Among many novel designs, microlattice structures are of prime interest to the research community (Bauer et al., 2017; Surjadi et al., 2019). Despite an extremely low relative density, these structures exhibit high stiffness and increased strength (Schwaiger et al., 2019). While metamaterials aim to surpass the behavior of natural materials, nature remains the epitome of pertinent and eloquent design. Imitating the

* Corresponding author.
E-mail addresses: kyriakos@me.berkeley.edu (K. Komvopoulos), cgrigoro@berkeley.edu (C.P. Grigoropoulos).

https://doi.org/10.1016/j.jmps.2020.104112
0022-5096/

Nomenclature

c_1, c_2	fit constants in Eq. (2)
$\boldsymbol{C}$	stiffness tensor
C_{ij}	components of stiffness vector
E	directional stiffness
$\bar{E}(=E/E_{\mathrm{b}})$	normalized stiffness in the [001] direction
E_{b}	bulk stiffness
L	length of a microlattice member
$\boldsymbol{M}$	state matrix depicting the arrangement of different unit cells in the microlattice structure
$\boldsymbol{n}$	direction vector of measured stiffness
n	number of unit cells or dimension of $\boldsymbol{x}$ vector and $\boldsymbol{M}$ matrix
P_{cr}	critical buckling load
r	radius of a microlattice member
S_{exp}	experimentally determined structure stiffness
S_{FEA}	numerically (FEA) determined structure stiffness
u_e	elastic strain energy density
$\boldsymbol{x}$	state vector of altered and removed microlattice members

Greek symbols

α	fit constant in Eq. (3)
β	fit constant in Eq. (3)
$\bar{\rho}$	relative density

Acronyms

A, B, C, D, E	unit cells representing five different states
FEA	finite element analysis
HIM	helium ion microscopy
IE	regular isohedron
MPL	multiphoton lithography
OT	octet truss
S, R, V	unchanged, rotated, and removed microlattice members, respectively
SEM	scanning electron microscopy
SB1, SB2, SB3	designs 1, 2, and 3 of modified structure with different unit cells, respectively
SP1, SP2, SP3	designs 1, 2, and 3 of modified structure with removed microlattice members, respectively

hierarchies observed in nature, microlattice structures embosom intriguing scale effects that significantly improve the mechanical behavior of the structure compared to the bulk material. Therefore, different structural designs that mimic living organisms have been fabricated at the microscale, demonstrating a significant enhancement of the mechanical performance (Luo and Greer, 2018; Zhang et al., 2020a). In addition, microlattices constructed by atomic layer deposition and plasma etching exhibit high ductility and resilience to large deformations, even when fabricated by brittle ceramic materials (Jang et al., 2013; Meza et al., 2014; Zhang et al., 2018; Zhang and Gu, 2020). The proliferation of the order of hierarchy in the structure can also embrace the same effect, increasing the resilience of the structure to large deformations (Meza et al., 2015). Moreover, tailoring the shape of these materials by various electrochemical processes may lead to distinct and uniform buckling modes, enabling on-demand control of the mechanical behavior (Xia et al., 2019).

The most critical factor dictating the mechanical performance of these structures is buckling, a state of structural instability that can lead to large deformations and catastrophic collapse of the material. Nevertheless, combined with post contact of the microlattice members, the buckling mechanism may result in structure densification and a significant increase of the stiffness and resilience to large deformations (Surjadi et al., 2019). Intertwined geometries inspired by the stellations of regular polyhedra have effectively utilized this effect through an increase in relative density and post contact of microlattice beam members instigated by buckling (Vangelatos et al., 2019a). This archetype has also been exploited in triply periodic foams (Al-Ketan et al., 2018). The length scale of unit cells may also display a significant effect on the mechanical behavior of microlattice structures. The buckling mechanisms of unit cells of various heights and microlattice diameters can differ significantly, leading to either egregious or functional mechanical responses (Vangelatos et al., 2019b).

Despite new categories of microscale metamaterials with exceptional mechanical properties, such as triply periodic and spinodal foams (Al-Ketan et al., 2018; Izard et al., 2019) or plate structures (Tancogne-Dejean et al., 2018; Chen et al., 2019a), these materials have yet to supersede microlattice structures. A major reason is that fabrication techniques with submicrometer resolution, such as diffusion-assisted high-resolution direct femtosecond laser writing (Sakellari et al., 2012), are highly efficient in performing three-dimensional (3D) linear laser scans, leading to the fabrication of microlattice members. However, fabricating more complex and bulky geometries becomes much more challenging due to voxel overlapping during

photopolymerization. Recent advances in mesoscale printing (Garcia-Taormina et al., 2019; Jonušauskas et al., 2019; Yang et al., 2019) might be instrumental in advancing the fabrication of large surface areas with microlattice beam members for emerging engineering applications. Topology optimization techniques have been thoroughly utilized to improve the performance of microlattice structures, leading to the development of structures that are not dictated by the Maxwell criterion for stretching dominated structures (Chen et al., 2019b).

Design oriented approaches have also been used to improve the performance of microlattice structures, specifically design strategies for modifying the crystal structure. Macrolattice structures consisting of different unit cells, such as BCC and FCC crystal lattices, have been developed (Pham et al., 2019) in which the morphology of grain boundaries has been elevated to larger scales. In addition, different unit cells placed at specific locations of the structure have been reported to function as interstitial or substitutional atoms, causing mechanical effects similar to hardening (Pham et al., 2019). Nevertheless, while this type of phase change may inspire novel designs, it does not evolve after the fabrication of the structures as the strengthening mechanisms of bulk materials.

Localized excessive plasticity and structure collapse resembling the formation of shear bands and slip planes has also been demonstrated for the aforementioned unit cells and also for simple octahedra (Qiu et al., 2015; Song et al., 2018). Nevertheless, these mechanisms are driven by the intricacies of 3D printing processes and native material defects of the fabricated structures (Qiu et al., 2015; Gautam and Idapalapati, 2019; Kudo et al., 2019; Song et al., 2018). Other design approaches for microlattice structures have been demonstrated at the microscale. More specifically, the removal of microlattice members to imitate vacancies or voids in the structure have been shown to influence the stiffness, strain energy density, localized plasticity, and structure collapse (Gross et al., 2019; Vangelatos et al., 2019c). However, effects such as those produced by dislocation avalanches (Hu et al., 2018), slip planes (Dimiduk et al., 2005), and substitutional atoms (Argon, 2008) have not been utilized to improve and tailor the mechanical behavior at the microscale. Furthermore, although succinct mechanics-oriented design approaches that increase the structural integrity have been employed to control the exact location of failure in the structure, they have not been used in conjunction with aforementioned approaches. Thus, these design methods have been tacitly explored for 3D microscale structures. These types of effects have not been exploited even at the macroscale with more conventional stretching or bending dominated unit cells, such as the octet truss (OT) (Deshpande et al., 2001) and the Kelvin unit cell (Meza et al., 2017). The fractography of these structures has also been limited because observing fracture nanofeatures in microlattices of a few hundred nanometers requires significantly high resolution. In addition, nonconductive materials, such as those used in multiphoton lithography (MPL), necessitate sputter-coating of a conductive film to enhance the image resolution, which may hinder important nanofeatures on fracture cross sections of the tested structure.

The principal objective of this study was to investigate how the mechanical properties of monolithic microlattices can be tailored by using designs inspired by crystal microstructures (Porter and Easterling, 1992; Argon, 2008; Pham et al., 2019). A finite element analysis (FEA) was performed to study how the directional stiffness of the material can be tailored on demand in specific directions. Results from in situ scanning electron microscopy (SEM)-nanoindentation investigations elucidate the effects of localized buckling and structure collapse on the stress-strain response. The OT structure, one of the most thoroughly studied mechanical metamaterials (Deshpande et al., 2001), was used to demonstrate how these principles can be manifested in the present design paradigm. Features causing localized failure at predetermined planes during large deformation that resemble slip-plane failure were introduced by changing the shape of select microlattice members. It is shown that further modification of these features can also lead to stiffening and enhanced resistance to failure. For example, it is proved that polycrystalline-like structures can be created by substituting the OT with modified structures inspired by the regular isohedron (IE) (Cromwell, 1997). Profoundly different deformation and failure mechanisms manifest themselves in the stress-strain response of each design. A dramatic increase of the mechanical integrity and strain energy density of the structure was observed even for fixed relative density, despite the removal of a significant number of microlattice members. High-depth focus imaging of the deformed structures performed by helium ion microscopy (HIM) provided insight into the deformation mode of internal unit cells. Results from fractography studies of the tested structures enabled by the extremely high resolution of HIM, even for nonconductive materials, further elucidated the mechanical behavior of the designed metamaterial structures.

2. Design principles and modeling of architected microlattice structures

Fig. 1 shows the design strategy scheme used to control mechanical failure and stiffening in a specific structure direction. Two design approaches were utilized to study the effects of architected defects and substitutional unit cells. In the first approach, an array of OT unit cells was altered either by the selective removal or alteration of specific microlattice beam members, whereas in the second approach, several OT unit cells were replaced by different unit cells, resulting in so-called different states. With both approaches, the objective was to control the directional stiffness of the structure and promote failure in predetermined regions of the structure (design cost functions). This was validated by stress analysis that revealed the existence of excess stress concentrations in the desired locations. Since performing multiple fabrications and mechanical testing is cumbersome and expensive, the former cost functions were studied by FEA. Consequently, the best structures were tested to validate the credibility of the design and FEA predictions. Nevertheless, it is instructive to provide a methodology of the design variables of the problem, i.e., the design inputs. A convenient method to analyze such a design problem is to use discrete qualitative variables (Zhang et al., 2020b), which do not express a physical quantity, such as length or angle,

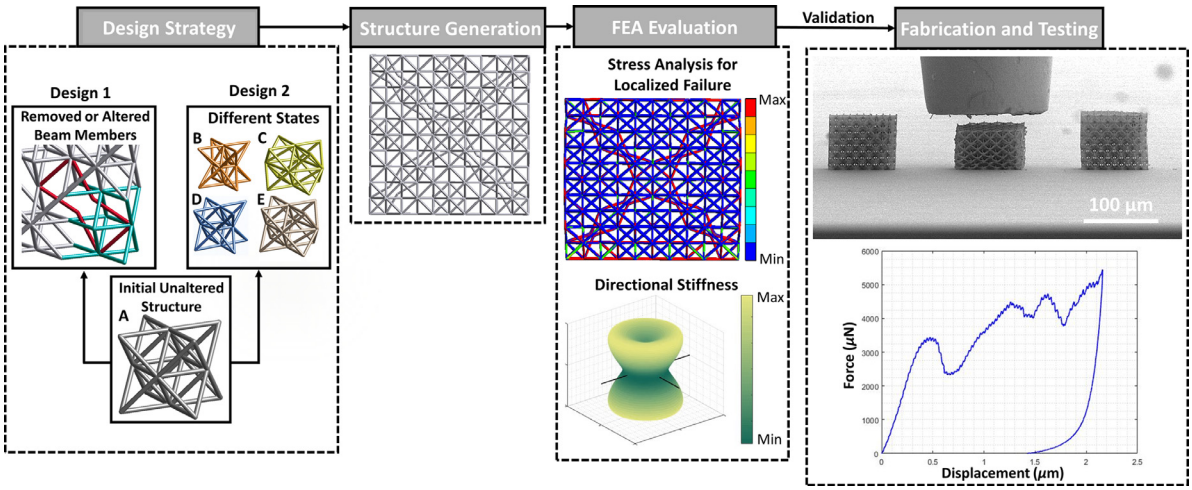

Fig. 1. Design strategy of metamaterial structures with architected microlattices. The design approach relies on introducing defects and substitutional unit cells in the structure by removing or altering beam members and by modifying unit cells in the array, respectively.

but different states of a variable, such as different surface treatments for enhancing the damage resistance of a material, for instance. Utilizing a similar methodology for the first design approach, each microlattice beam member was unchanged, altered in various ways, or removed. The OT unit cell comprises 36 beam members. However, proximal unit cells of an array share the beam members at their common faces. Thus, the total number of microlattice beam members in an $n \times n$ array of OT unit cells is equal to $36n^2 - 8(n-1)$. This equation is different for other types of unit cells, such as the Kelvin unit cell (Meza et al., 2017), because it depends on the number of beam members at the common faces of the unit cells. To reduce the complexity of the problem, the structures were made symmetric with respect to the horizontal and vertical middle planes, thus reducing the number of design variables to $9n^2 - 2(n-1)$. Consequently, the number of beam elements is represented by a vector $\boldsymbol{x}$ in which each beam element has a state designated by S, R, or V, depending on the geometrical configuration of the structure. State S indicates unchanged beam members, state R corresponds to beam members rotated to form a bowtie structure, and state V refers to beam members removed from the unit cell. Characteristic beam members with S or R state are shown in Fig. 1 in blue and red color, respectively. These different states are also exemplified in the structures shown in Fig. S1 of the Supplementary Information (SI). For the second design approach, a unit cell in the array was left unchanged or substituted by a different unit cell structure, i.e., states A, B, C, etc., depending on the number of different states. Therefore, for this design paradigm, an $n \times n$ matrix $\boldsymbol{M}$ with unit cell elements at different states was used to mathematically depict the structure. This type of formulation has been utilized to represent discrete states of a system in a qualitative way (Zhang et al., 2020b) and is further interpreted in the discussion section. As mentioned earlier, 5×5 arrays were designed to be symmetric with respect to the horizontal and vertical middle planes, reducing the design space to 25 design variables. Each design variable represents five potential different unit cells (i.e., five states) that are labeled by A, B, C, D, and E in Fig. 1. These states are also discernible in the structures shown in Fig. S2 of the SI. More details about the origin of different states are given below.

To examine the effect of different states on the mechanical performance of the structure, different test structures were modeled and fabricated. Fig. 2 shows the designs of the metamaterial structures examined in this study. The unit cell of the original structure is the OT (Fig. 2A). The first design category includes structures SP1 (Fig. 2B), SP2 (Fig. 2C), and SP3 (Fig. 2D) with modified unit cells integrated as bowtie two-dimensional (2D) structures at the $\pm 45°$ diagonal planes of the structures. The microlattice members of the bowties change the symmetry of the internal octahedron of each OT that they surmount. The difference between the SP1 and the SP2 structure is that the bowtie in the latter structure has an internal microlattice member connecting its central nodes. The purpose of the SP1 design was to facilitate larger deformations of the bowtie microlattice members causing contact of the beam members during deformation, which is known to increase the stiffness and energy density of the structure (Gibson and Ashby, 1997; Chen et al., 2019a; Vangelatos et al., 2019a). The SP3 structure has the same bowtie design as the SP1 structure; however, several beam members were removed from the $\pm 45°$ planes containing the bowtie microlattices to promote buckling in these planes. Several microlattice beam members of the SP3 structure were also removed from locations proximal to the diagonal planes to enable the structure to sustain its own weight during the fabrication, while still demonstrating the desired deformation. More details about the design of the SP1, SP2, and SP3 structures are given in the SI, and magnified schematics of the modified regions of these structures are shown in Fig. S1. These structures belong to the first design group and their $\boldsymbol{x}$ vectors are given in the SI.

Another major objective of this study was to develop designs that increase the stiffness of the structure in predetermined directions. Thus, the second design category includes structures SB1 (Fig. 2E), SB2 (Fig. 2F), and SB3 (Fig. 2G). For these structures, instead of modifying the beam members of the unit cells, the OT structure was substituted by variations of

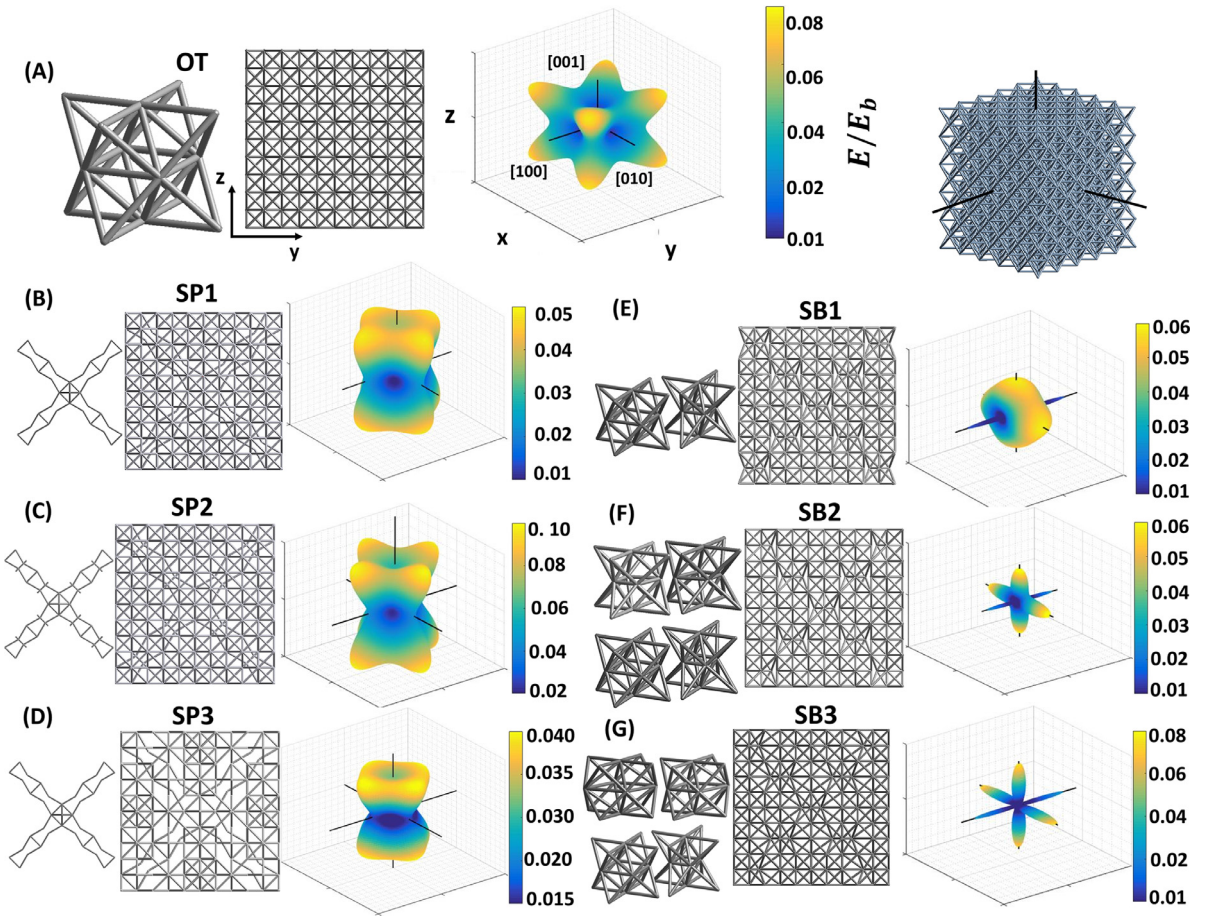

Fig. 2. Design and effective stiffness of metamaterial structures. (A) The OT structure (unit cell, front view, effective stiffness map, and 3D configuration). (The Cartesian directions shown in the stiffness map and the 3D schematic of the OT are the same for all structures.) Front views of (B–D) SP1, SP2, and SP3 structures and (E–G) SB1, SB2, and SB3 structures illuminating structural modification details and corresponding effective stiffness maps. The unit cells of the former structures are shown on the left of their front views. All the design modifications yield significant changes in directional stiffness, particularly a profound stiffness increase in the [001] direction of all structures compared to the OT structure.

the regular IE (Cromwell, 1997) and the unit cells were positioned at the same positions of the modified OT unit cells in the first design category. The reason for selecting the IE is that the size and shape of each of its faces matches those of the OT, thus alleviating the design process. Besides the convenient incorporation of the IE in the unit cell array, the IE is also characterized by a much higher critical buckling load than the OT. Indeed, an eigenvalue buckling analysis showed that the critical buckling load of the IE is 38.8% higher than that of the OT. As shown in the next section, this structural enhancement can be augmented by positioning the IE at specific locations of the OT array. The unit cells in the SB1, SB2, and SB3 structures mimic lattice voids, which, as shown later, enable contact of the microlattice members in the OT array during the deformation of the structure. All of the structure architectures in the second design category imitate the distortion of a crystal lattice by substitutional atoms of various atomic radii (Porter and Easterling, 1992; Argon, 2008). While the SB1 structure has the OT and one variation of the IE only, the SB2 structure has the OT and two different unit cells. The difference between the SB2 and the SB3 structure is that the faces of the modified unit cells in the SB3 structure are connected to neighboring unit cells, as opposed to the substitutional unit cells in the SB2 structure that are not connected with the faces of neighboring unit cells. Further details about the structures of the second design category are provided in the SI, and the exact location of each modified unit cell can be seen in Fig. S2. The mathematical formulation of the matrix $\boldsymbol{M}$ of the SB1, SB2, and SB3 structures is given in the SI. Although other potential locations of either defect or substitutional unit cells can be considered, in this study we demonstrate the improved mechanical performance in the planes of maximum shear stress of the compressed bulk material (Porter and Easterling, 1992). As shown below, for some of the designs this leads to a profound increase in localized buckling and plastic deformation at the $\pm 45^{\circ}$ planes, leading to failure mechanisms that resemble shear band formation (Qiu et al., 2015; Song et al., 2018; Pham et al., 2019).

In the present study, it was selected to increase the stiffness of the structure in the [001] direction, as confirmed by the effective stiffness maps shown in Fig. 2. Although there are other directions of higher stiffness, such as the [111] direction,

for the vast majority of previous studies, the [001] orientation was used to fabricate OT structures (Zheng et al., 2014; Bauer et al., 2015; Meza et al., 2014, 2017; Mieszala et al., 2017; Zhang et al., 2018; 2019; Al-Ketan et al., 2018; Gross et al., 2019; Kudo et al., 2019). In addition, experimental results do not show a significant improvement of the stiffness in the [111] direction compared to the [001] direction (Zheng et al., 2014).

To obtain the effective stiffness map of each structure, the directional stiffness of the material $E(\boldsymbol{n})$ was computed by

$$E(\boldsymbol{n}) = \frac{1}{(\boldsymbol{n}\otimes\boldsymbol{n}) : \boldsymbol{C}^{-1}(\boldsymbol{n}\otimes\boldsymbol{n})}, \tag{1}$$

where $\boldsymbol{n}$ is an arbitrary direction in the structure and $\boldsymbol{C}$ is the stiffness vector. The details about the derivation of Eq. (1) can be found in the SI.

For a valid comparison of the mechanical performance of the architected structures, it was necessary to fix the relative density. To accomplish this, the CADs of each structure were designed with the FEA code ANSYS and their relative density $\bar{\rho}$ was curve fitted using the relation (Meza et al., 2017),

$$\bar{\rho} = c_1\left(\frac{r}{L}\right)^2 + c_2\left(\frac{r}{L}\right)^3, \tag{2}$$

where r and L are the radius and the length of each microlattice beam member, respectively, and c_1 and c_2 are constants determined by curve fitting. The quadratic term represents the summation of the volume of each individual beam over the volume of the bulk material; however, this term does not take into account the overlapping of the beams at the nodes and, therefore, tends to overestimate the relative density. Thus, the cubic term is used to correct the calculation of the relative density for this additional volume. In the CAD designs, the overlap beam volume was not included in the calculation of the total volume. The fitting parameters of each structure are given in Table S1 of the SI. Using the obtained equations of the relative density, all of the samples were designed to have a relative density $\bar{\rho} = 0.025$, which is also the lowest relative density for preventing structure collapse during fabrication. The relative density was controlled by either modulating the laser power or the velocity of the fabrication stage. For $\bar{\rho} \approx 0.025$, the beam radius was not found to vary significantly, which increased the fabrication robustness. In all of the designs examined in this study, the beam length was set at $8\,\mu$m.

To obtain the stiffness tensor of each structure, $5 \times 5 \times 4$ unit cell arrays subjected to different loading conditions were analysed with the ANSYS code (select simulation results are shown in Fig. S3 of the SI). An approach that provides highly accurate results of the macroscopic stiffness of the structure (Tan et al., 2000; Xu et al., 2016) was used in the FEA. Nevertheless, in the present study the stiffness tensor does not refer to the tensor of an equivalent continuum but the stiffness of discrete microlattice structures, as reported previously (Zheng et al., 2014; Xu et al., 2016). Obtaining the equivalent continuum stiffness tensor requires variational approaches (Yildizdag et al., 2019), which can greatly increase the modeling complexity of the structures. Because of its cubic symmetry, the stiffness tensor of the OT includes three independent constants; however, the distortion promulgated by the modified and substitutional unit cells leads to symmetry loss at one orthogonal plane, elevating the symmetry to tetragonal and increasing the number of independent constants to six. While the cubic symmetry could have been preserved by applying the same 2D modification to other orthogonal planes of the structure, it was decided to keep the modification at planes easily viewed during testing. Further details about the calculation of the stiffness components and FEA modeling can be found in the SI. The calculated components of the stiffness tensor C_{ij} of each structure are given in Table S2 of the SI. A 3D polar plot of the normalized stiffness $\bar{E} = E/E_b$ (where E_b is the bulk stiffness) of each structure is also shown in Fig. 2. All of the modified structures possess stiffness maps profoundly different from that of the OT structure. In particular, while the maximum stiffness of the OT structure is in the [111] direction, the stiffness maps of the SP1, SP2, and SP3 structures are rotated with respect to the [001] direction and are more uniform in the plane normal to the [001] direction, whereas the maximum stiffness of the SB1, SB2, and SB3 structures has been transcended to the [001] and [010] directions.

Fig. 3 shows the normalized stiffness $\bar{E}$ in the [001] direction of all tested structures versus the relative density. Because some structures show an increase in stiffness slope with relative density due to several beams coming into contact, the normalized stiffness is expressed as

$$\bar{\mathrm{E}} = \alpha\bar{\rho}^p + \beta\bar{\rho}^q \tag{3}$$

where α, β, p, and q are fitting parameters. While similar models have been used in fatigue to distinguish plastic from elastic behavior, the power p and q parameters in Eq. (3) distinguish proximal from intersecting microlattice members. Fig. S4 of the SI illustrates how this geometrical change arises as the radius-to-length ratio is varied. The fitting parameters in Eq. (3) were obtained from an FEA of all the structures for various relative densities and are given in Table S3 of the SI. As shown in Fig. 3, except of the SP3 structure, the stiffness of all other structures having $\bar{\rho} > 0.03$ is higher than that of the OT structure, even by a factor as high as 2.12 (SB3 structure). The noticeably higher relative stiffness of the SP2, SB2, and SB3 structures than the other structures is attributed to the highest connectivity of microlattice members in the former designs. The result that the SP3 structure is stiffer than the OT structure for $\bar{\rho} < 0.03$ is consonant with reported results showing that the selective removal of beam members from predefined locations can improve the mechanical properties of lattice structures (Gross et al., 2019; Vangelatos et al., 2019c). Inevitably, the mechanical response of the bulk material becomes prevalent with the significant increase of the relative density (Gibson and Ashby, 1997).

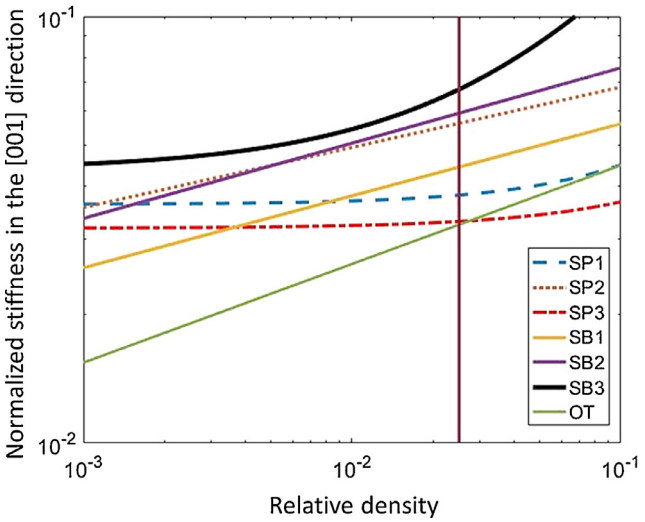

Fig. 3. Normalized stiffness in the [001] direction versus relative density of metamaterial structures. With the only exception of the SP3 structure, the stiffness of all other structures is significantly higher than that of the OT structure. The vertical line indicates the relative density ($\bar{\rho} = 0.025$) of the tested structures.

3. Experimental procedures

Each structure was fabricated by a modified MPL process, known as diffusion-assisted high-resolution direct femtosecond laser writing (Sakellari et al., 2012), which enables the fabrication of microstructures with nanoscale features. Further details about the experimental setup and materials can be found in the SI. The dimensions of the architected structures were selected so that all of them to have the same relative density as in the simulations (i.e., $\bar{\rho} = 0.025$), the only exception being the SP3 structure, which had a slightly lower relative density (i.e., $\bar{\rho} = 0.022$) because it comprised fewer microlattice members. The average beam radius in each structure was modulated by changing the laser power to achieve the desired relative density. However, at this length scale the MPL produces polymerized ellipsoid voxels that are not perfectly orbicular. To mitigate this effect, the laser beam was scanned four times along the same path to increase the thickness of the voxel in the radial direction. In addition, to ensure that the fabricated structures were devoid of this fabrication constraint, apart from SEM imaging, experimental and simulation results were contrasted and the differences were found to be insignificant. Fig. 4 shows characteristic SEM images of the fabricated structures. All of the structures consist of $5 \times 5 \times 4$ arrays of unit cells, matching the geometry of the structures used in the FEA. Structure modification is indicated by the different morphologies of neighboring unit cells, such as those for the SB1 structure seen in Fig. 4A. The voids created by the IE can be observed in Fig. 4B, with the magnified view shown in Fig. 4C revealing that proximal unit cells do not share the same face. Fig. 4D shows a 3D image of the SP3 structure, which is the only structure with some of its microlattice members removed, while Fig. 4E shows a region from where a few microlattice members were removed (shown by red dot lines). Fig. 4F shows a front view of the SP3 structure, which allowed viewing the evolution of various deformation modes during mechanical testing.

The mechanical tests were performed with a nanoindenter mounted inside an SEM (Hysitron P188 SEM PicoIndenter, Bruker). All of the structures were positioned such that their frontal faces to be observable, similar to the front views of the structures shown in Figs. 2 and 4. This allowed a frame-by-frame analysis of the video recordings to provide the location and instant of localized deformation events. All of the structures were deformed in compression to 50% of their undeformed height. At least 8 specimens of each structure were tested to ensure the repeatability of the experimental results. Further information about the mechanical testing procedure can be found in the SI.

4. Results

Fig. 5 shows a representative force versus displacement response of the SP3 structure. The flat block seen at the top of the structure (also in similar SEM images of following force-displacement plots) is the rigid flat tip. These SEM images and Video S1 showing a full load/unload cycle of the SP3 structure reveal several characteristic deformation stages. Subsequently to the engagement of the flat tip with the structure (Fig. 5A), a fairly linear force response emerged with the gradual increase of the load, indicative of the overall elastic behavior of the structure, until the occurrence of a noticeable change in force slope at a load of $\sim$2500 μN (Fig. 5B) that was prompted by localized buckling of a few microlattice members (shown in red enclosures). This occurrence produced intense force fluctuations, attributed to the collapse of the $+45^\circ$ diagonal plane of the structure, shown by the large red enclosure (Figs. 5C and 5D), involving twisting of the central unit cell (the red circle in Fig. 5C). The maximum stress drop due to the collapse of the $+45^\circ$ plane of the structure is $\sim$1.88 MPa. (The details

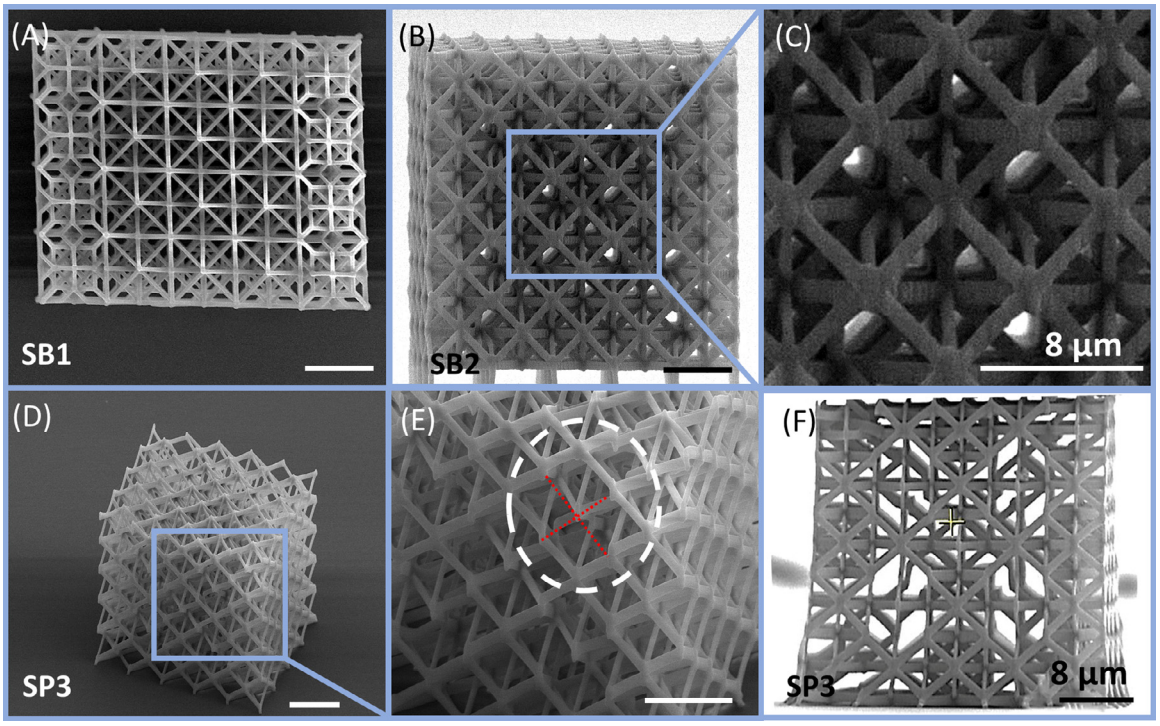

Fig. 4. Characteristic SEM micrographs of the SB1, SB2, and SP3 metamaterial structures. (A) Top view of the SB1 structure showing the modified unit cells at the edges. (B) Front view of the SB2 structure. (C) High-magnification image of an individual unit cell of the SB2 structure showing the orientation of neighboring microlattice members. (D) Side view of the SP3 structure. (E) High-magnification image of a side array of the SP3 structure showing the locations where a few microlattice members (red dot lines) were removed. (F) Front view of the SP3 structure. All structures have a relative density equal to ~0.025, except the SP3 structure that has a relative density of 0.022. The scale bar in all the SEM images is equal to 8 μm.

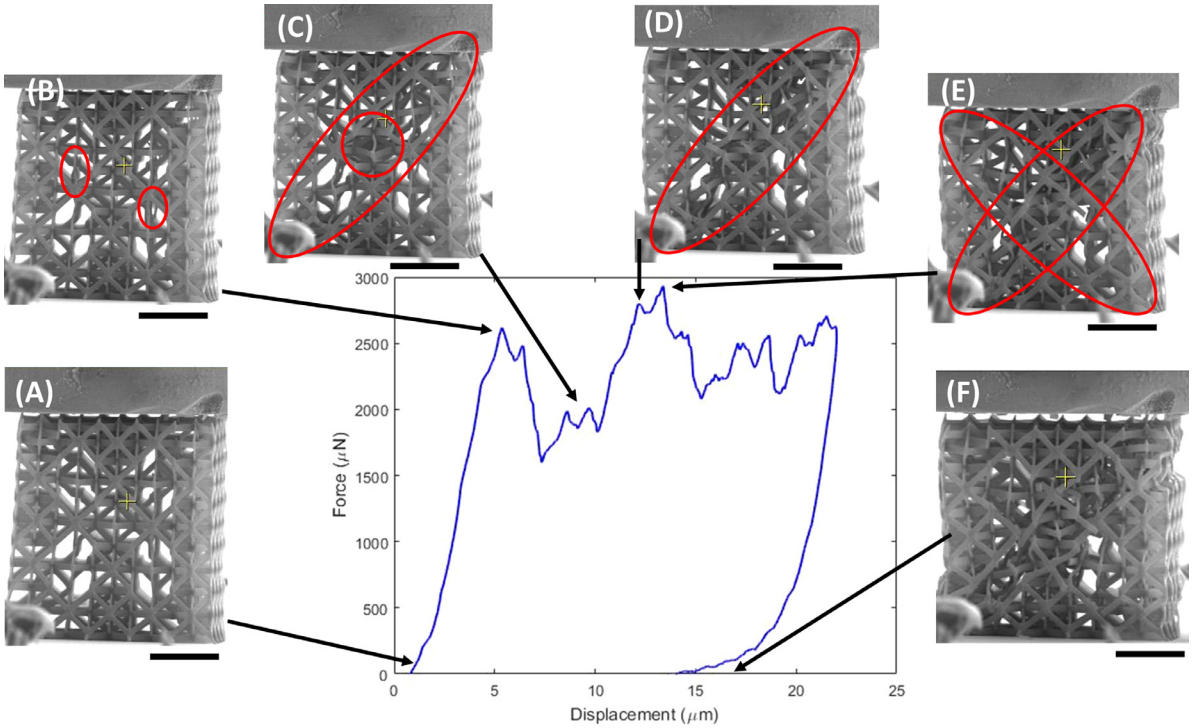

Fig. 5. Force versus displacement response of the SP3 metamaterial structure. Characteristic deformation stages (A–F) were determined from SEM images and Video S1 of a load/unload cycle. After the flat tip was brought into contact with the top face of the structure (A), a notable change in force slope was observed as the load was gradually increased due to localized buckling of some microlattice members (enclosed by red circles) (B). This was followed by excessive deformation of the microlattice members at the +45° diagonal plane (enclosed by an ellipsoid) with the central unit cells (enclosed by red circles) exhibiting torsional deformation (C), resulting in structure densification and stiffening. With the further increase of the load, localized fracture was instigated on the +45° diagonal plane (D) and soon after on the –45° diagonal plane (E). Unloading revealed excessive deformation of the microlattice members at both diagonal planes, especially the unit cells at the plane edges (F). The scale bar in all the SEM images is equal to 10 μm.

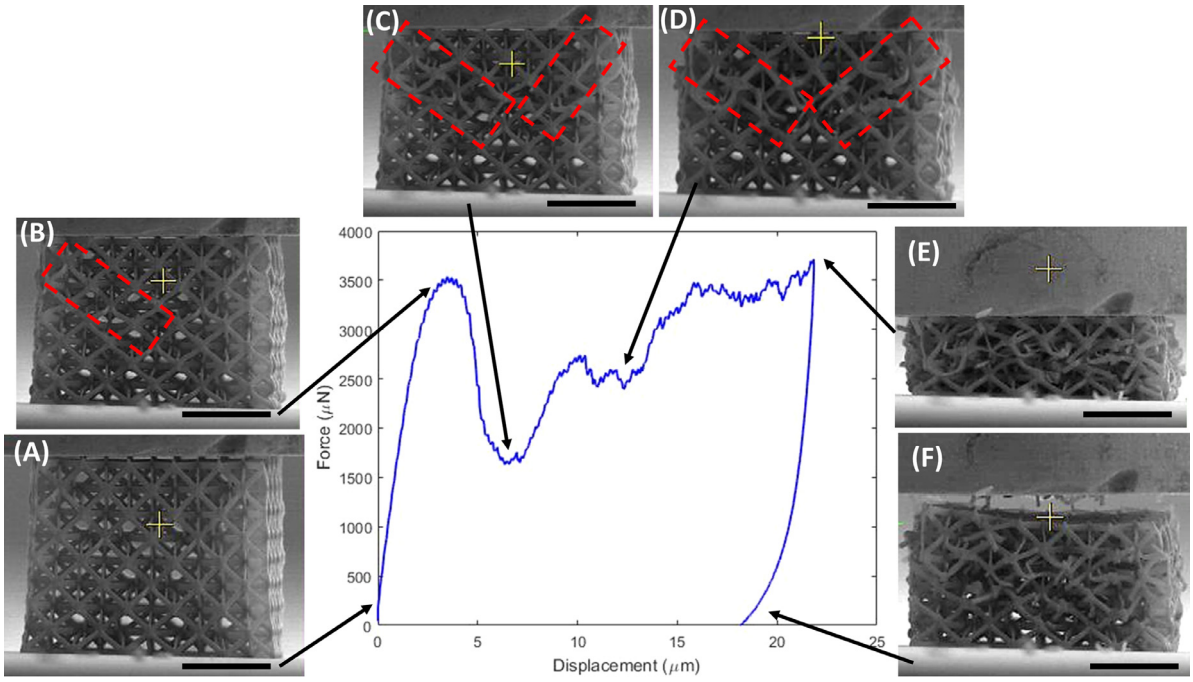

Fig. 6. Force versus displacement response of the SB2 metamaterial structure. Characteristic deformation stages (A–F) were determined from SEM images and Video S2 of a full load/unload cycle. After the engagement of the flat tip with the top face of the structure (A) and the gradual increase of the load, excessive deformation of microlattice members (enclosed by dashed red lines) occurred in the −45° diagonal plane, resulting in beam buckling (B). With the further increase of the load, large deformations were instigated in the mirror +45° diagonal plane of the structure (C), afterwards leading to the collapse and fracture of both diagonal planes (D). Further loading propelled the collapse of several layers of the structure (E). Unloading revealed the global collapse of the structure. The scale bar in all the SEM images is equal to 16 μm.

of the conversion of the force-displacement data to stress-strain data are given in the SI.) After a small increase of the deformation, the mirrored (−45°) diagonal plane of the structure also collapsed (Fig. 5E). Unloading of the SP3 structure revealed that localized deformation at the ±45° planes of the structure also deformed slightly the unit cells at the center of the plane edges (Fig. 5F). The marginally asynchronous collapse of the diagonal planes of the structure is attributed to the imperfect alignment of the flat tip with the top face of the structure. The initiation of microlattice beam collapse at the diagonal planes activated the rapid failure of additional beam members at these planes, similar to the generation of localized failures generated by a dislocation avalanche (Csikor et al., 2007; Hu et al., 2018). The foregoing phenomenon differs significantly from the collapse of a whole layer of the structure and the proliferation of damage to the underlying layers encountered with other designs. The localized failure in the diagonal plane of the SP3 structure is also supported by the FEA results shown in Fig. S3C of the SI.

Fig. 6 shows a representative force versus displacement response of the SB2 structure. Again, SEM imaging and Video S2 of a full load/unload cycle of the SB2 structure reveal several characteristic deformation stages. After the tip was brought into contact with the top face of this structure (Fig. 6A) and the load was gradually increased, buckling of the beams in several unit cells at the −45° diagonal plane (enclosed by red dashed lines) was instigated at a load of ∼3500 μN (Fig. 6B), which is much higher than that of structure SP3 (Fig. 5). However, collapse failure commenced at the +45° diagonal plane (Figs. 6C and 6D). For this structure, the collapse did not propagate to the lower half of the structure as for the SP3 structure; instead, the bottom layers of the structure exhibited fairly uniform deformation (Figs. 6E and 6F). Again, stress fluctuations occurred in the post yield regime of the stress-strain curve, with average stress drops just before the instigation of buckling being equal to ∼0.29 MPa. At the top of the first stress peak (Fig. 6B) the stress drop is equal to 0.46 MPa and demonstrates fluctuations of high repetition rate. However, when the whole −45° diagonal plane collapsed, the stress fluctuation repetition decreased and the stress drop decreased back to 0.29 MPa (Fig. 6C). Another difference is that failure at the diagonal plane of the SP3 structure was not uniform. Instead, it comprised localized buckling and collapse leading to the failure of proximal beam members. Conversely, uniform failure of each diagonal plane as a whole occurred in the SB2 structure. This explains the relatively less intense force fluctuations in the mechanical response of the SB2 structure (Fig. 6). The FEA results of the SB2 structure shown in Fig. S3E of the SI reveal high stresses along the ±45° diagonal planes for the vast majority of the beam members comprising these unit cells.

Fig. 7 shows a representative force versus displacement response of the OT structure. Several characteristic deformation stages were identified by SEM imaging and by observing the deformation of the structure during a full load/unload cycle recorded in Video S3. Ensuing the engagement of the tip with the OT structure (Fig. 7A) and after the gradual increase of

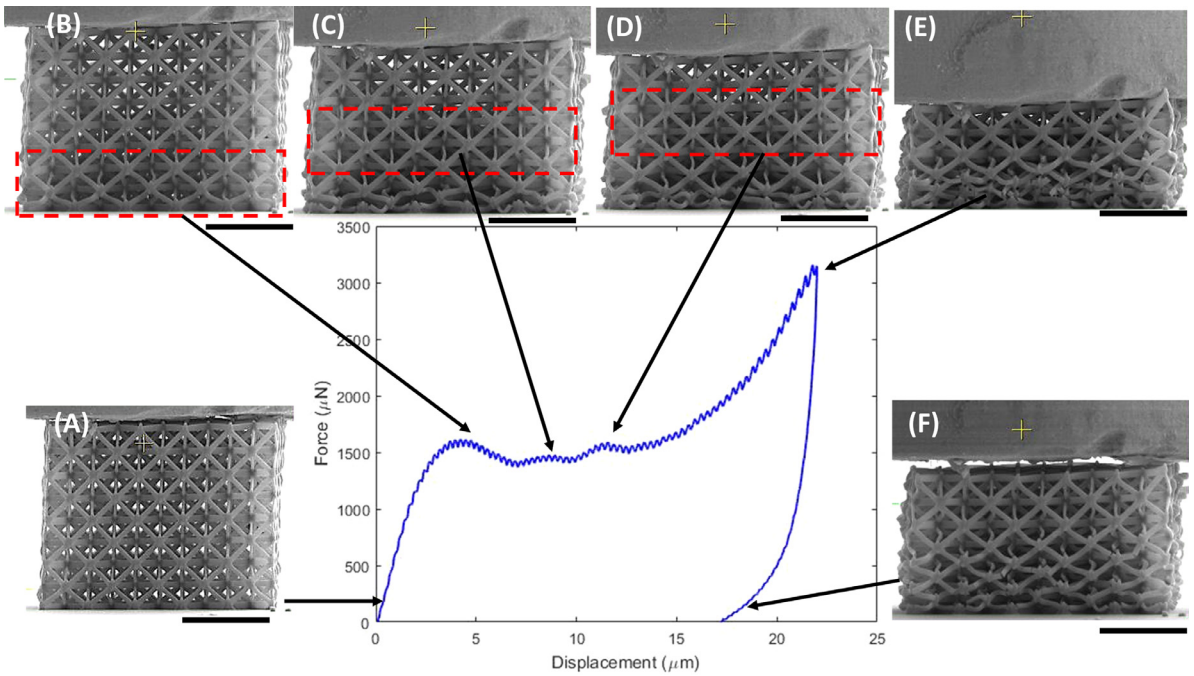

Fig. 7. Force versus displacement response of the OT metamaterial structure. Characteristic deformation stages (A–F) were determined from SEM images and Video S3 of a full load/unload cycle. After the engagement of the flat tip with the top face of the structure (A) and the gradual increase of the load, buckling of microlattice members (enclosed by dashed red lines) was instigated at the bottom layer of the structure leading to its collapse (B). The further increase of the load resulted in the catastrophic collapse of subsequent layers (enclosed by dashed red lines) of the structure (C–E). Unloading revealed the total collapse of the bottom layers (F). The scale bar in all the SEM images is equal to 10 μm.

Table 1
Stiffness, critical buckling load, and elastic strain energy density of metamaterial structures.

Structure	Stiffness		Critical buckling load P_{cr} (μN)	Elastic strain energy density u_e (J/cm^3)
	S_{exp} (MPa)	S_{FEA} (MPa)		
SP1	113.07 ± 5.36	108.16	3385 ± 32	2.04 ± 0.18
SP2	172.04 ± 7.56	162.06	4241 ± 130	2.07 ± 0.28
SP3	85.65 ± 5.13	91.44	2230 ± 57	1.60 ± 0.15
SB1	125.04 ± 8.32	128.77	4375 ± 63	4.67 ± 0.33
SB2	182.97 ± 8.24	172.51	3527 ± 108	2.14 ± 0.21
SB3	139.02 ± 46.67	202.55	3649 ± 45	2.65 ± 0.05
OT	98.72 ± 3.05	95.65	1607 ± 98	0.69 ± 0.08

the load, a profound change in force slope occurred at a load of ~1600 μN due to localized buckling of the beam members comprising the octahedra of the OT unit cells at the bottom layers (enclosed by red dashed lines in Fig. 7B). This was succeeded by the uniform collapse of other layers of the structure, consistent with the findings of previous studies (Meza et al., 2014, 2015; Zheng et al., 2014; Jang et al., 2013; Mieszala et al., 2017; Zhang et al., 2018). Similar to the previous structures, the OT structure also exhibited a serrated stress-strain response in the post yield regime. The commencement of instability and plastic deformation resulted in an average stress drop of ~0.16 MPa before the first stress peak, and after exhibiting softening, it reached a steady state of ~0.51 MPa through the whole loading at high repetition rate. Instead of the abrupt changes in force slope of the SP3 and SB2 structures observed after the first buckling event, the evolution of structural damage in the OT structure densified the regions with fractured members (Figs. 7C–7E), resembling a ductile behavior, with the structure exhibiting a catastrophic collapse characterized by distributed damage (Gibson and Ashby, 1997). A uniform collapse of the layers of the lower half of the structure was observed upon full unloading (Fig. 7F). The FEA results shown in Fig. S3G of the SI demonstrate high stresses at the bottom layer, which can be correlated to the subsequent collapse of the bottom layer.

Characteristic force-displacement responses of other metamaterial structures are shown in Figs. S5–S8 of the SI. The mechanical behaviors of these structures reveal similar characteristics with those shown in Figs. 5–7. Statistical experimental and FEA results of the structural stiffness, S_{exp} and S_{FEA}, respectively, critical buckling load, P_{cr} , and elastic strain energy density, u_e, are given in Table 1. The stiffness and strain energy density were calculated from the initial elastic response of the structures, i.e., before the instigation of the first buckling event. The results show that the stiffness, critical buckling load,

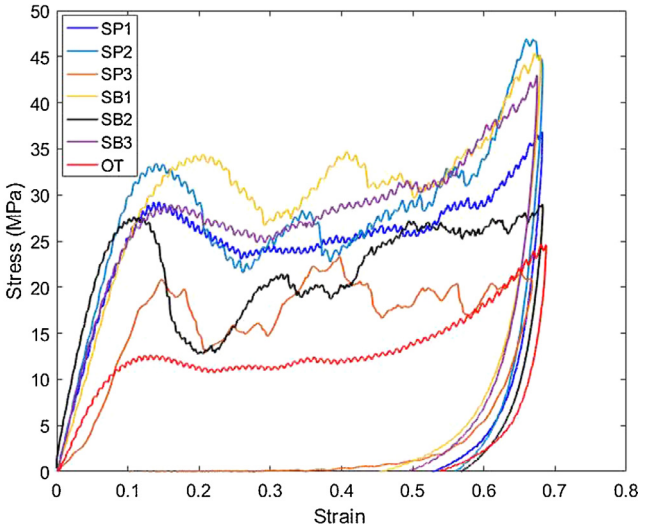

Fig. 8. Stress-strain responses of metamaterial structures. The results indicate commensurate augmentation of the stiffness and strain energy density of all architected structures compared to the OT structure. The stress-strain responses of all structures are characterized by multiple regions of structural instability and post yield stress fluctuations, whereas the densification of the collapsed OT structure resembles macroscopic hardening, mitigating the buckling instabilities observed with the collapse of subsequent layers in the architected structures.

and strain energy density of all structures are higher than those of the OT structure, the only exception being the stiffness of the SP3 structure that is attributed to its fewer microlattice members. However, despite the higher critical buckling load of the structures, not all of them embrace the design objective of localized failure, because the collapse of subsequent layers in some of the structures resembled the deformation mode of the OT structure; nevertheless, the stress-strain responses shown in Fig. 8 reveal a remarkably improved mechanical behavior even for these designs. All of the structures demonstrate significantly higher strain energy density than the OT structure, indicated by the larger hysteresis area of the corresponding stress-strain response. To compare the mechanical performance of each structure, the experimental data are contrasted in Fig. 9. The numerical values of the statistical data of all structures are given in Table 1. Fig. 9A shows that the critical buckling load of all structures is higher than that of the OT structure by as much as 172% (SB1 structure). The SP3 structure shows the lowest increase in critical buckling load, i.e., 38% higher than that of the OT structure. Nonetheless, this is still a notable improvement considering the significantly fewer microlattice members of the SP3 structure, which intuitively would suggest a lower buckling load. This shows that tactical and concinnated placement of defects and substitutional unit cells can increase the structure resilience to collapse. For post contact of microlattice members to effectively increase the energy dissipation and stiffness of structures with intertwined geometries, buckling must commence in the early stage of deformation (Vangelatos et al., 2019a,b). However, for structures that lack intertwined microlattices, buckling promotes fracture of the beam members. Hence, for structures with microlattice members that do not exhibit post contact during deformation, buckling must be forestalled to enhance the structure's resilience to catastrophic failure. Fig. 9B shows the elastic stain energy density of each structure calculated as the area under the stress-strain response up to the instigation of buckling. The elastic strain energy density increased with the buckling load. Most notably, the SB1 structure demonstrated a strain energy density 577% higher than that of the OT structure. The main reason for this result is that the neighboring IE and OT unit cells do not share the same faces; consequently, at large deformations, they come into contact, stiffening the structure and preventing collapse during the initial stage of deformation. The strain energy density of the SP3 structure is 132% higher than that of the OT structure, which is counterintuitive considering its lower relative density. Fig. 9C shows a comparison between the structure stiffness measured in the [001] direction during the initial stage of elastic deformation with the structural stiffness obtained from the FEA simulations also for the [001] direction. The close agreement between experimental and simulation results validates the effective stiffness maps (Fig. 2). The only structure showing a significant difference between experimental and FEA effective stiffness in the [001] direction is the SB3 structure. This disagreement is most likely due to imperfections in contact between the flat tip and the top face of the SB3 structure, as indicated by the large standard deviation of the measurements of this structure alone. The SB2 and SP3 structures showed the highest and lowest experimental stiffness, i.e., higher by 85.65% and 13% than that of the OT structure, respectively. It is noted that in addition to a higher stiffness, the SP3 structure demonstrated a better structural integrity and higher strain energy dissipation capacity than the OT structure, despite its lower relative density.

Further insight into the mechanical behavior of the designed microlattice structures was provided by fractography results of fractured microlattice members. Despite the large deformations caused by buckling and the macroscopic mechanical behavior resembling ductile behavior, the microlattice beams incurred sudden fracture. Because the beam diameter was equal to $\sim$125 nm in all structures, a significantly higher imaging resolution was necessary for capturing the morphological features on fracture cross sections. In addition, it was riveting to reveal the internal failure of the structures to further elucidate

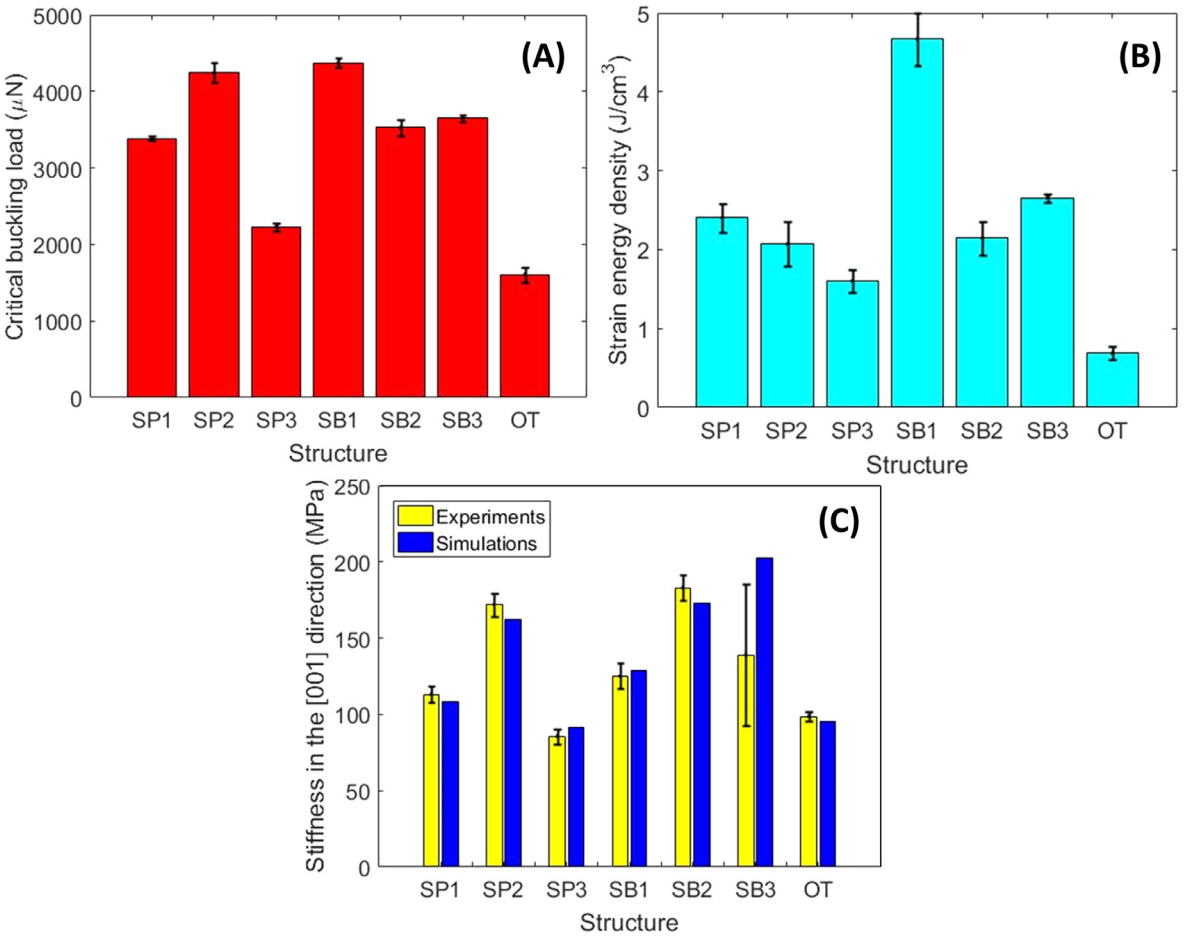

Fig. 9. Experimental and FEA simulation results of the mechanical performance of metamaterial structures with fixed relative density ($\bar{\rho} = 0.025$). (A) Critical buckling load at the instigation of the first buckling event. All structures show a higher buckling load than that of the OT structure, indicating a significant enhancement of their structural integrity. (B) Strain energy density of each structure computed as the area under the stress-strain curve up to the first instant of buckling. The significant increase in elastic strain energy density exhibited by all architected structures is attributed to the increase of the critical buckling load and the post contact behavior of proximal microlattice members in some of the designs. (C) Comparison of experimental and simulation results of the structure stiffness in the [001] direction. Apart from the SP3 structure which, despite having fewer beam members, showed approximately the same stiffness with the OT structure, all other structures demonstrated significantly higher stiffness.

the 3D deformation of failed microlattice members. This was accomplished by HIM imaging. This technique does not require the deposition of a conductive surface layer, which may alter the surface micro/nanomorphology, and provides high depth of focus that enables the observation of the internal layers of the structure and features as small as a few nanometers. Characteristic HIM images of deformed, buckled, and fractured microlattice members located in the interior of the SP1 and SB3 structures are shown in Fig. 10. Figs. 10A and 10B show that buckling of microlattice members contributed to excessive deformation and twisting of the unit cells. The twisting mode of deformation was not captured in the linear FEA of the structures, presumably because of the manifestation of effects encountered at micrometer length scales that are associated with higher order deformation gradient terms in the constitutive relation (Yildizdag et al., 2019). While these models may capture the observed mechanical response, they have not been used to analyze 3D microlattice structures because of their high complexity. In addition, the twisting deformation suggests that the microlattice members reached the post yield regime and the structure evolved to exhibit a ductile behavior. Nevertheless, the occurrence of fracture in a few hundred microseconds (captured in the video recordings) resembles brittle behavior and is supported by the high-resolution fractography images shown in Figs. 10C and 10D, which illuminate the absence of discernible roughness (texture) and dimple formation. These features together with the fibril formation observed in Fig. S9 of the SI indicate the commencement of brittle fracture caused by crazing (Deblieck et al., 2011). Crazing occurs when an excessive tensile stress is exerted to a polymer, leading to microvoid nucleation and fibril formation at the crack front. Buckling of microlattice members led to the development of tensile stresses at one side of the beams that caused microcracking, as seen in Figs. 10C and 10D and Fig. S9 of the SI. Considering the photoresist used to fabricate the metamaterial structures is classified as polymeric-ceramic hybrid, this failure mode matches the evidence derived from the HIM images.

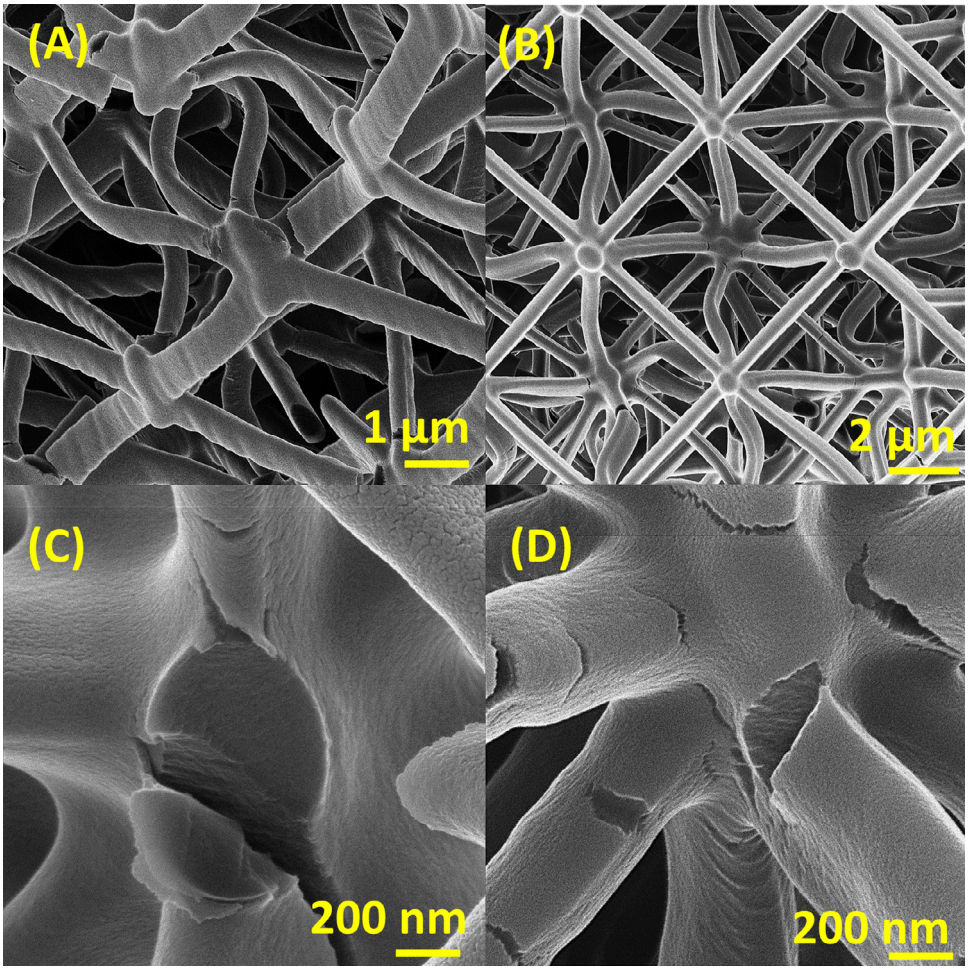

Fig. 10. High-magnification images of fractured regions in SP1 and SB3 metamaterial structures obtained with a helium ion microscope. (A) Tilted view of fractured beam members in the SP1 structure revealing excessive deformation propelled by localized buckling. (B) Top view of a tested SB3 structure showing torsional deformation of the beams of internal layers and localized microcracking activated after buckling. (C) Characteristic fracture cross section of the SP1 structure. Despite the large deformation induced by buckling resembling ductile behavior, the lack of dimple formation on the fractured cross-sectional area and the extensive microcracking indicate brittle fracture due to crazing. (D) High-magnification image of the intersection of several microlattice members in the SB3 structure. Microcracking and the lack of texture (roughness) in the fractured cross sections indicate the dominance of brittle fracture.

5. Discussion

The increased stiffness, critical buckling load, and elastic strain energy density demonstrated by the architected microlattice structures are attributed to the tailored defects and substitutional unit cells introduced in the OT unit cells. The uniqueness of these enhancing mechanisms is that they lead to localized deformation at predetermined locations of the structure, promoting either post contact that leads to stiffening or inherent stiffening, as shown by the stiffness maps obtained by the FEA. In addition, the directional stiffness of the OT structure obtained with an analytical approach (Abdelhamid, 2017) was found to be in fair agreement with the FEA results of this study.

Although the present designs enhanced the mechanical performance in the [001] direction, other modifications can be employed to improve the performance in other directions. The intriguing result observed with the SEM is that localized buckling leads to a collapse avalanche or uniform layer-by-layer failure. These mechanical behaviors have been inspired by and aimed to resemble mechanisms that strengthen and control failure in bulk materials (Porter and Easterling, 1992; Argon, 2008). It is well established that defects affect the dislocation mobility and substitutional atoms cause hardening. The present study shows that their microscale equivalents can accomplish similar effects. While localized failure mimics dislocation movement or grain boundary failure, hardening is reflected by the higher stain energy density of the material and the increased resilience to buckling and fracture. Despite the fact that the deformation mode of the examined microlattice structures illuminates ductile behavior, the HIM images and video recordings revealed that the fracture behavior was actually brittle. Considering the previous work with intertwined metamaterial structures that provided insight into brittle-to-ductile

transition (Vangelatos et al., 2019a), it may be inferred that utilizing these types of unit cells can potentially enhance the mechanical performance even more. Consequently, different unit cells or defects may further improve the performance of microlattice structures. For example, plate structures demonstrate the same stiffness in all directions (Tancogne-Dejean et al., 2018).

Another interesting finding of this study is the different characteristics of the serrated force-displacement (stress-strain) profiles of the SP3, SB2, and OT structures. (The SP1, SP2, SB1, and SB3 structures demonstrated serrated stress profiles similar to that of the OT structure.). The SP3, SB2, and OT structures showed significantly different serrated stress profiles. Despite the fact that this mechanical trait was precipitated by means different from those of bulk materials, the stress patterns resemble bulk material behavior due to Portevin-Le Chatelier bands resulting from nonuniform plastic flow (Chihab et al., 1987). The regular stress fluctuations and high stress drops resembling type C bands (Chihab et al., 1987) demonstrated by the SP3 structure are attributed to an avalanche mechanism. The initially small number of collapsing microlattice members activated an abrupt collapse of beams at the -45° diagonal plane of the SP3 structure. Conversely, the SB2 structure yielded irregular stress fluctuations and smaller stress drops than the SP3 structure. The stress irregularity displayed by the SB2 structure was instigated by a change in collapse direction, evidenced by the uniform collapse of the -45° diagonal plane, the sequential collapse of the $+45^\circ$ diagonal plane, and, finally, the collapse of the bottom layer. The small stress fluctuations are attributed to the cumulative effect of buckling instabilities and beam microcracking events at both diagonal planes before the instigation of uniform beam failure at the diagonal planes. In a bulk material, such stress drops are classified as type A (Chihab et al., 1987). The OT structure demonstrated regular stress fluctuations and fixed stress drops resembling type B (Chihab et al., 1987). This behavior may be associated with a steady layer-by-layer collapse without changing direction. Again, the small stress drops may be ascribed to the agglomeration of instabilities and beam microcracking in each collapsing layer. It is noted that the SP3 structure did not collapse because of the concurrent instigation of microcracks along the diagonal planes but because of the increase of microfracturing events during deformation. While these mechanisms commence in bulk materials at different strain rates (Chihab et al., 1987), the underlying reason for the incidence of these mechanisms in the tested structures was the structure architecture. Therefore, it may be argued that introducing architected defects in metamaterial structures provides an effective means for controlling the development of plasticity.

Although more complex polyhedral structures can be designed, increasing the array of structures also increases the complexity of the design. To overcome this difficulty, optimization tools, such as deep learning (Ma et al., 2018) and topology optimization (Chen et al., 2019b), can be instrumental in the design of metamaterial structures exhibiting a specific performance and even isotropic behavior. Nevertheless, topology optimization requires the use of continuous quantitative design variables and thus far has led to the design of monolithic lattice structures (Chen et al., 2018; 2019b). Importantly, such optimization techniques are sensitive to the size of the design space. In previous studies of architected materials that utilized optimization methods, such as deep learning (Ma et al., 2018), machine learning (Daghigh et al., 2020; Kim et al., 2020; Zhang and Gu, 2020), and Bayesian optimization (Zhang et al., 2020b), it was reported that using either qualitative or quantitative variables requires tens of thousands of initial random data to explore and exploit the design space and obtain the optimum structure, even for design spaces smaller than those of the present study (Daghigh et al., 2020; Zhang et al., 2020b). Therefore, such optimization methods can be effective when the simulations can be automated and performed expeditiously. However, the selective removal or alteration of microlattice beam members and the connectivity of different neighboring unit cells requires high computational time to design arrays of structures. Furthermore, if the cost functions that need to be minimized are related to a post yield or fracture material parameter, the computational cost to solve the boundary value problem of such complex arrays will be unaccountably high. The present study promulgates the necessity to develop optimization techniques necessitating a small number of data points that can be achieved with considerably lower computational cost. These tools are essential for optimizing complex 3D structure problems involving discrete non-monolithic lattices of large arrays. To further elucidate the intriguing complex deformation and fracture mechanisms of architected structures, more advanced modeling tools (Fraternali and Amendola, 2017), such as the Kirchhoff rod theory (Davi, 1992), may be incorporated in the design methodology. The FEA simulations of this study revealed the initial evolution of stresses in the structures, illuminating the most likely locations of plastic deformation and microfracture. The simulation results qualitatively portrayed where failure may commence and did not require prohibitively expensive computation. To elucidate the post yield mechanical response, elastic-plastic FEA analyses accounting for the evolution of localized fracture must be performed, significantly increasing the computational cost of the design analysis. Therefore, elastic material parameters should be used as proxy functions to improve the performance of the structure beyond the elastic regime and evaluate these intuitive results through experiments. Nevertheless, predicting instabilities due to localized buckling and microfracture from FEA simulations will provide further insight into their contribution to the stress drops observed in the post yield regime and avalanche collapse mechanisms. Therefore, future work should also focus on minimizing the computational cost of such simulations.

Considering that scale effects that reveal brittle-to-ductile transitions have been reported (Mieszala et al., 2017; Vangelatos et al., 2019b), performing fractography studies of architected structures designed at different length scales may yield invaluable insight into the scale-dependent deformation of mechanical metamaterials, providing impetus for the development of sophisticated FEA models. Because the observed localized failure mechanisms occurred in a few hundred nanometers and within a few hundred microseconds, high-resolution SEM imaging was critical to characterizing the de-

forming structures. This investigation has shown that combining in situ SEM-nanoindentation, fast video recording, and high-resolution HIM imaging provides an effective methodology for studying deformation and microcracking processes at length scales of a few nanometers. Moreover, considering the significant enhancement of the mechanical performance of the microlattice structures examined in this study, it is imperative to extend the applicability of the MPL process to larger structure dimensions. Rapid fabrication of such architected structures on surfaces extending to several centimeters, while preserving nanometer-scale features, may facilitate metamaterial developments spanning a wide range of applications, such as structural materials, bio-implants, and even 3D tissue scaffoldings. Recent advances in mesoscale printing and 3D focal-field engineering are important steps toward this goal and the design of metamaterial structures with superior and controllable mechanical properties.

6. Conclusions

A new design strategy was developed in this study by introducing hybrid microlattice structures augmented with strengthening mechanisms that resemble those of crystal materials. The novelty of the designed architected structures is rooted in two principles. First, the tactical removal or alteration of microlattice members, inspired by defects observed in slip planes, aimed to control localized deformation at predetermined positions and, ultimately, enhance the structure properties. Second, the incorporation of substitutional unit cells that distort the symmetry of the microlattice structure in proximal regions, precipitating the same effects as the first design principle.

FEA simulations revealed how the directional stiffness of the structure can be increased in predetermined locations and directions, whereas in situ SEM-nanoindentation experiments with structures fabricated by a modified MPL process revealed how the microscopic (localized) mechanical response manifests itself into the significant increase of the stiffness, strain energy density and overall mechanical integrity of the structure. Thus, a noteworthy finding of this study is how the mechanical behavior of microlattice structures consisting of stiff and strong metamaterial structures can be significantly improved compared to their monolithic counterparts. Another valuable contribution of this work is the insight into the complex deformation modes of internal unit cells accomplished by HIM imaging, particularly the illumination of large deformations that resemble ductile behavior and fracture mechanisms associated with crazing. From a more general perspective, the present investigation introduced a new methodology for modifying the mechanical behavior of 3D microlattices, furnishing 3D artificial defects and unit cells in strategic locations of the array of the architected structure.

Declaration of Competing Interest

The authors have no conflicts of interest to disclose.

CRediT authorship contribution statement

Z. Vangelatos: Conceptualization, Data curation, Formal analysis, Investigation, Methodology, Software, Validation, Visualization, Writing - original draft, Writing - review & editing. **K. Komvopoulos:** Investigation, Supervision, Validation, Writing - original draft, Writing - review & editing. **C.P. Grigoropoulos:** Funding acquisition, Project administration, Resources, Supervision, Validation, Writing - review & editing.

Acknowledgments

This work was partially funded by the National Science Foundation under the Scalable Nanomanufacturing Program, Award No. 1449305. The nanoindentation, SEM, and HIM experiments were carried out at the California Institute of Quantitative Bioscience (QB3 Lab). The authors thank Professor P. Hosemann, Department of Nuclear Engineering, University of California, Berkeley (UCB), for the use of the nanoindentation apparatus, Dr. F. Allen, Department of Materials Science and Engineering (UCB) for training to use the helium ion microscope, and Professor L. Pruitt, Department of Mechanical Engineering (UCB) for discussions about the fractography results.

Supplementary Information

Additional information associated with this article can be found in the online version under Supplementary Information (SI) at doi:10.1016/j.jmps.2020.104112.

References

Abdelhamid, M., 2017. Effective Mechanical Properties of 3D Structural Materials, MS Thesis. York University, Toronto, Ontario, Canada.
Al-Ketan, O., Rezgui, R., Rowshan, R., Du, H., Fang, N.X., Al-Rub, R.K.A., 2018. Microarchitected stretching-dominated mechanical metamaterials with minimal surface topologies. Adv. Eng. Mater. 20, 1800029.
Argon, A.S., 2008. Strengthening Mechanisms in Crystal Plasticity. Oxford University Press, New York, NY.
Bauer, J., Meza, L.R., Schaedler, T.A., Schwaiger, R., Zheng, X., Valdevit, L., 2017. Nanolattices: an emerging class of mechanical metamaterials. Adv. Mater. 29, 1701850.

Bauer, J., Schroer, A., Schwaiger, R., Tesari, I., Lange, C., Valdevit, L., Kraft, O., 2015. Push-to-pull tensile testing of ultra-strong nanoscale ceramic–polymer composites made by additive manufacturing. Extreme Mech. Lett. 3, 105–112.
Berezovski, A., Yildizdag, M.E., Scerrato, D., 2020. On the wave dispersion in microstructured solids. Continuum Mech. Thermodyn. 32, 569–588.
Chen, D., Skouras, M., Zhu, B., Matusik, W., 2018. Computational discovery of extremal microstructure families. Sci. Adv. 4, eaao7005.
Chen, W., Watts, S., Jackson, J.A., Smith, W.L., Tortorelli, D.A., Spadaccini, C.M., 2019b. Stiff isotropic lattices beyond the Maxwell criterion. Sci. Adv. 5, eaaw1937.
Chen, Z., Xie, Y.M., Wu, X., Wang, Z., Li, Q., Zhou, S., 2019a. On hybrid cellular materials based on triply periodic minimal surfaces with extreme mechanical properties. Mater. Des. 183, 108109.
Chihab, K., Estrin, Y., Kubin, L.P., Vergnol, J., 1987. The kinetics of the Portevin-Le Chatelier bands in an Al-5at%Mg alloy. Scripta Metal. 21, 203–208.
Csikor, F.F., Motz, C., Weygand, D., Zaiser, M., Zapperi, S., 2007. Dislocation avalanches, strain bursts, and the problem of plastic forming at the micrometer scale. Science 318, 251–254.
Daghigh, V., Lacy Jr., T.E., Daghigh, H., Gu, G., Baghaei, K.T., Horstemeyer, M.F., Pittman Jr., C.U., 2020. Machine learning predictions on fracture toughness of multiscale bio-nano-composites. J. Reinf. Plast. Compos. 39, 587–598.
Davi, F., 1992. The theory of Kirchhoff rods as an exact consequence of three-dimensional elasticity. J. Elasticity 29, 243–262.
Deblieck, R.A.C., van Beek, D.J.M., Remerie, K., Ward, I.M., 2011. Failure mechanisms in polyolefines: the role of crazing, shear yielding and the entanglement network. Polymer 52, 2979–2990.
Deshpande, V.S., Fleck, N.A., Ashby, M.F., 2001. Effective properties of the octet-truss lattice material. J. Mech. Phys. Solids 49, 1747–1769.
Dimiduk, D.M., Uchic, M.D., Parthasarathy, T.A., 2005. Size-affected single-slip behavior of pure nickel microcrystals. Acta Mater. 53, 4065–4077.
Fraternali, F., Amendola, A., 2017. Mechanical modeling of innovative metamaterials alternating pentamode lattices and confinement plates. J. Mech. Phys. Solids 99, 259–271.
Garcia-Taormina, A.R., Juarez, T., Oakdale, J.S., Biener, J., Hodge, A.M., 2019. Scaling-up of nano-architected microstructures: a mechanical assessment. Adv. Eng. Mater. 21, 1900687.
Gautam, R., Idapalapati, S., 2019. Compressive properties of additively manufactured functionally graded Kagome lattice structure. Metals 9, 517.
Gibson, L.J., Ashby, M.F., 1997. Cellular Solids: Structure and Properties, 2nd ed Cambridge University Press, Cambridge, UK.
Cromwell, P.R., 1997. Polyhedra. Cambridge University Press, Cambridge, UK.
Gross, A., Pantidis, P., Bertoldi, K., Gerasimidis, S., 2019. Correlation between topology and elastic properties of imperfect truss-lattice materials. J. Mech. Phys. Solids 124, 577–598.
Hu, Y., Shu, L., Yang, Q., Guo, W., Liaw, P.K., Dahmen, K.A., Zuo, J.-M., 2018. Dislocation avalanche mechanism in slowly compressed high entropy alloy nanopillars. Commun. Phys. 1, 61.
Izard, A.G., Bauer, J., Crook, C., Turlo, V., Valdevit, L., 2019. Ultrahigh energy absorption multifunctional spinodal nanoarchitectures. Small 15, 1903834.
Jang, D., Meza, L.R., Greer, F., Greer, J.R., 2013. Fabrication and deformation of three-dimensional hollow ceramic nanostructures. Nature Mater. 12, 893–898.
Jonušauskas, L., Gailevičius, D., Rekštyte, S., Baldacchini, T., Juodkazis, S., Malinauskas, M., 2019. Mesoscale laser 3D printing. Opt. Express 27, 15205–15221.
Kim, Y., Yang, C., Kim, Y., Gu, G.X., Ryu, S., 2020. Designing an adhesive pillar shape with deep learning-based optimization. ACS Appl. Mater. Interf. 12, 24458–24465.
Kudo, A., Misseroni, D., Wei, Y., Bosi, F., 2019. Compressive response of non-slender octet carbon microlattices. Front. Mater. 6, 169.
Luo, S., Greer, J.R., 2018. Bio-mimicked silica architectures capture geometry, microstructure, and mechanical properties of marine diatoms. Adv. Eng. Mater. 20, 1800301.
Ma, W., Cheng, F., Liu, Y., 2018. Deep-learning-enabled on-demand design of chiral metamaterials. ACS Nano 12, 6326–6334.
Meza, L.R., Das, S., Greer, J.R., 2014. Strong, lightweight, and recoverable three-dimensional ceramic nanolattices. Science 345, 1322–1326.
Meza, L.R., Phlipot, G.P., Portela, C.M., Maggi, A., Montemayor, L.C., Comella, A., Kochmann, D.M., Greer, J.R., 2017. Reexamining the mechanical property space of three-dimensional lattice architectures. Acta Mater. 140, 424–432.
Meza, L.R., Zelhofer, A.J., Clarke, N., Mateos, A.J., Kochmann, D.M., Greer, J.R., 2015. Resilient 3D hierarchical architected metamaterials. Proc. Nat. Acad. Sci. USA 112, 11502–11507.
Mieszala, M., Hasegawa, M., Guillonneau, G., Bauer, J., Raghavan, R., Frantz, C., Kraft, O., Mischler, S., Michler, J., Philippe, L., 2017. Micromechanics of amorphous metal/polymer hybrid structures with 3D cellular architectures: size effects, buckling behavior, and energy absorption capability. Small 13, 1602514.
Pham, M.-S., Liu, C., Todd, I., Lertthanasarn, J., 2019. Damage-tolerant architected materials inspired by crystal microstructure. Nature 565, 305–311.
Porter, D.A., Easterling, K.E., 1992. Phase Transformations in Metals and Alloys, 2nd ed CRC Press, Boca Raton, FL.
Qiu, C., Yue, S., Adkins, N.J.E., Ward, M., Hassanin, H., Lee, P.D., Withers, P.J., Attallah, M.M., 2015. Influence of processing conditions on strut structure and compressive properties of cellular lattice structures fabricated by selective laser melting. Mater. Sci. Eng. A 628, 188–197.
Sakellari, I., Kabouraki, E., Gray, D., Purlys, V., Fotakis, C., Pikulin, A., Bityurin, N., Vamvakaki, M., Farsari, M., 2012. Diffusion-assisted high-resolution direct femtosecond laser writing. ACS Nano 6, 2302–2311.
Schwaiger, R., Meza, L.R., Li, X., 2019. The extreme mechanics of micro- and nanoarchitected materials. MRS Bull. 44, 758–765.
Song, J., Gao, L., Cao, K., Zhang, H., Xu, S., Jiang, C., Surjadi, J.U., Xu, Y., Lu, Y., 2018. Metal-coated hybrid meso-lattice composites and their mechanical characterizations. Compos. Struct. 203, 750–763.
Surjadi, J.U., Gao, L., Du, H., Li, X., Xiong, X., Fang, N.X., Lu, Y., 2019. Mechanical metamaterials and their engineering applications. Adv. Eng. Mater. 21, 1800864.
Tan, P., Tong, L., Steven, G.P., 2000. Behavior of 3D orthogonal woven CFRP composites. Part II. FEA and analytical modeling approaches. Composites: Part A 31, 273–281.
Tancogne-Dejean, T., Diamantopoulou, M., Gorji, M.B., Bonatti, C., Mohr, D., 2018. 3D plate-lattices: an emerging class of low-density metamaterial exhibiting optimal isotropic stiffness. Adv. Mater. 30, 1803334.
Vangelatos, Z., Melissinaki, V., Farsari, M., Komvopoulos, K., Grigoropoulos, C., 2019a. Intertwined microlattices greatly enhance the performance of mechanical metamaterials. Math. Mech. Solids 24, 2636–2648.
Vangelatos, Z., Gu, G.X., Grigoropoulos, C.P., 2019b. Architected metamaterials with tailored 3D buckling mechanisms at the microscale. Extreme Mech. Lett. 33, 100580.
Vangelatos, Z., Komvopoulos, K., Grigoropoulos, C.P., 2019c. Vacancies for controlling the behavior of microstructured three-dimensional mechanical metamaterials. Math. Mech. Solids 24, 511–524.
Xia, X., Afshar, A., Yang, H., Portela, C.M., Kochmann, D.M., Di Leo, C.V., Greer, J.R., 2019. Electrochemically reconfigurable architected materials. Nature 573, 205–213.
Xu, S., Shen, J., Zhou, S., Huang, X., Xie, Y.M., 2016. Design of lattice structures with controlled anisotropy. Mater. Des. 93, 443–447.
Yang, D., Liu, L., Gong, Q., Li, Y., 2019. Rapid two-photon polymerization of an arbitrary 3D microstructure with 3D focal field engineering. Macromol. Rapid Commun. 40, 1900041.
Yildizdag, M.E., Tran, C.A., Spagnuolo, M., Barchiesi, E., dell'Isola, F., Hild, F., 2019. A multi-disciplinary approach for mechanical metamaterial synthesis: a hierarchical modular multiscale cellular structure paradigm. In: Altenbach, H., Öchsner, A. (Eds.), State of the Art and Future Trends in Material Modeling, Vol. 100, Springer, Switzerland, pp. 485–505.
Zhang, X., Wang, Y., Ding, B., Li, X., 2020a. Design, fabrication, and mechanics of 3D micro-/nanolattices. Small 16, 1902842.
Zhang, Y., Apley, D.W., Chen, W., 2020b. Bayesian optimization for materials design with mixed quantitative and qualitative variables. Sci. Rep. 10, 4924.
Zhang, Z., Gu, G.X., 2020. Finite-element-based deep-learning model for deformation behavior of digital materials. Adv. Theory Simul. 3, 2000031.

Zhang, X., Yao, J., Liu, B., Yan, J., Lu, L., Li, Y., Gao, H., Li, X., 2018. Three-dimensional high-entropy alloy–polymer composite nanolattices that overcome the strength–recoverability trade-off. Nano Lett. 18, 4247–4256.
Zhang, X., Vyatskikh, A., Gao, H., Greer, J.R., Li, X., 2019. Lightweight, flaw-tolerant, and ultrastrong nanoarchitected carbon. Proc. Nat. Acad. Sci. USA 116, 6665–6672.
Zheng, X., Lee, H., Weisgraber, T.H., Shusteff, M., DeOtte, J., Duoss, E.B., Kuntz, J.D., Biener, M.M., Ge, Q., Jackson, J.A., Kucheyev, S.O., Fang, N.X., Spadaccini, C.M., 2014. Ultralight, ultrastiff mechanical metamaterials. Science 344, 1373–1377.